Journal of Advanced Ceramics
2022, **11**(5): 729–741
https://doi.org/10.1007/s40145-022-0566-6
ISSN 2226-4108
CN 10-1154/TQ

Research Article

Realizing enhanced energy storage and hardness performances in $0.90NaNbO_3$–$0.10Bi(Zn_{0.5}Sn_{0.5})O_3$ ceramics

Xiaoyan DONG[a], Xu LI[b], Hongyun CHEN[a], Qinpeng DONG[a], Jiaming WANG[a], Xiang WANG[a], Yue PAN[a], Xiuli CHEN[a,*], Huanfu ZHOU[a]

[a]*Collaborative Innovation Center for Exploration of Hidden Nonferrous Metal Deposits and Development of New Materials in Guangxi*, *Key Laboratory of Nonferrous Materials and New Processing Technology*, *Ministry of Education*, *School of Materials Science and Engineering*, *Guilin University of Technology*, *Guilin 541004*, *China*
[b]*College of Materials Science and Engineering*, *Sichuan University*, *Chengdu 610064*, *China*

Received: July 28, 2021; Revised: November 9, 2021; Accepted: January 8, 2022

Abstract: Ceramic dielectric capacitors have a broad scope of application in pulsed power supply devices. Relaxor behavior has manifested decent energy storage capabilities in dielectric materials due to its fast polarization response. In addition, an ultrahigh energy storage density can also be achieved in $NaNbO_3$ (NN)-based ceramics by combining antiferroelectric and relaxor characteristics. Most of the existing reports about lead-free dielectric ceramics, nevertheless, still lack the relevant research about domain evolution and relaxor behavior. Therefore, a novel lead-free solid solution, $(1-x)NaNbO_3$–$xBi(Zn_{0.5}Sn_{0.5})O_3$ (abbreviated as xBZS, x = 0.05, 0.10, 0.15, and 0.20) was designed to analyze the domain evolution and relaxor behavior. Domain evolutions in xBZS ceramics confirmed the contribution of the relaxor behavior to their decent energy storage characteristics caused by the fast polarization rotation according to the low energy barrier of polar nanoregions (PNRs). Consequently, a high energy storage density of 3.14 J/cm^3 and energy efficiency of 83.30% are simultaneously available with 0.10BZS ceramics, together with stable energy storage properties over a large temperature range (20–100 ℃) and a wide frequency range (1–200 Hz). Additionally, for practical applications, the 0.10BZS ceramics display a high discharge energy storage density (W_{dis} ≈ 1.05 J/cm^3), fast discharge rate ($t_{0.9}$ ≈ 60.60 ns), and high hardness (H ≈ 5.49 GPa). This study offers significant insights on the mechanisms of high performance lead-free ceramic energy storage materials.

Keywords: energy storage; $NaNbO_3$ (NN)-based; domain evolutions; hardness

1 Introduction

Dielectric capacitors have a broad scope of applications in pulsed power supply devices via the virtue of their large power density, rapid charge/discharge rates, and long cycle lifetime [1,2]. The low energy storage densities, however, limit their further development toward miniaturization and integration. Normally, the energy storage performances (ESP) of dielectric capacitors can be described via Eqs. (1)–(3) [3–5]:

$$U_{rec} = \int_{P_r}^{P_{max}} E\mathrm{d}P \quad (1)$$

* Corresponding author.
E-mail: cxlnwpu@163.com

$$U = \int_0^{P_{max}} E\mathrm{d}P \quad (2)$$

$$\eta = \frac{U_{rec}}{U} \times 100\% \quad (3)$$

where P_{max}, P_r, E, U_{rec}, U, and η are the maximum polarization, remanent polarization, applied electric field, recoverable energy storage density, overall energy storage density, and energy storage efficiency, respectively. Ideal dielectric capacitors with high U_{rec} values should have a high dielectric breakdown electric field (E_b) and a large polarization difference ($\Delta P = P_{max} - P_r$). Meanwhile, for practical applications, there are usually lattice defects (such as defect dipoles, ion vacancies, interstitial atoms, etc.) and brittleness caused by strong ionic bonds in dielectric ceramic capacitors. These defects are usually accompanied by cracks and partial discharges under an external electric field, thereby affecting the breakdown characteristics of dielectric materials. In addition, as structural components, ceramic capacitors will also suffer different static forces during assembly and use. These forces can also cause ceramic capacitors to crack [6,7]. Therefore, these ceramics require adequate hardness characteristics to reduce the possibility of cracking.

To achieve a high E_b and a large $\Delta P = P_{max} - P_r$, various types of dielectric capacitors, such as linear dielectrics (LD), ferroelectrics (FE), relaxor ferroelectrics (RFE), and anti-ferroelectrics (AFE), have been developed [8–11]. Among these materials, LDs usually possess considerable E_b and η, but rarely achieve large U_{rec} because of their low dielectric constants [8]. FEs have problems caused by their dielectric nonlinearities and large P_r. Therefore, pure $BaTiO_3$ and $Bi_{0.5}Na_{0.5}TiO_3$ are not conducive to achieving excellent energy storage characteristics [12]. Unlike LDs and FEs, RFE and AFE ceramics have been widely reported to exhibit acceptable energy storage performance owing to their relatively large ΔP values [13,14]. $NaNbO_3$ (NN) ceramics, as representative AFEs, are potential to be commercialized due to its high dielectric constant, wide band gap energy, absence of potassium element, and low volume density [15]. Nevertheless, owing to the slight difference in free energy, the metastable FE phase ($P2_1ma$) and AFE phase ($Pbma$) of NN ceramics could coexist at room temperature (RT). When the applied electric field is removed, the ferroelectric phase induced by the electric field can still be observed, which is unfavorable for obtaining excellent energy storage characteristics [16]. Subsequently, much research has focused on how to stabilize the AFE phase by doping some ABO_3 perovskites that have a lower tolerance factor or polarizability. For instance, Ye *et al*. [17] confirmed that the introduction of $CaSnO_3$ boosts the antiferroelectricity of NN ceramics by measurements with the X-ray diffraction (XRD) patterns, transmission electron microscopy (TEM) images, and Raman spectra. Similarly, a typical double hysteresis loop is also observed in other $NaNbO_3$–$CaZrO_3$ systems [18]. Most NN AFE solid solutions, nevertheless, still present large hysteresis and non-zero P_r, which limits its further application in the field of energy storage. Recent studies have shown that the combination of relaxor features and AFE phase can effectively optimize the AFE to FE phase transition of NN-based ceramics, thereby significantly optimizing energy storage characteristics. For example, through constructing antiferroelectric and relaxor characteristics, Ye *et al*. [19] achieved both a large U_{rec} of 2.8 J/cm^3 and a high E_b of 300 kV/cm in 0.9NN–0.1BMN ceramics. Qi *et al*. [14] acquired a superhigh U_{rec} of 12.2 J/cm^3 at 0.76NN–0.24BNT relaxor antiferroelectric ceramics. Although there are some reports of achieving large U_{rec} and η simultaneously for NN-based solid solutions, the internal mechanisms of excellent energy storage characteristics, such as domain evolution and visualized relaxor behavior, are rarely reported for most NN-based ceramics. In addition, owing to the relatively low density and large pore size, the hardness characteristics of NN-based ceramics receive little attention, which reduces their reliability and lifetime in practical applications.

In this work, we chose $Bi(Zn_{0.5}Sn_{0.5})O_3$ as the dopant to study the above problems. On one hand, the AFE phase can be stabilized via decreasing the tolerance factor [20]. Based on the equation of the tolerance factor: $t = (R_A + R_O)/[\sqrt{2}(R_B + R_O)]$ (where R_A, R_B, and R_O are the average ionic radii of the A-site cation, B-site cation, and oxygen anion, respectively; Na^+ (1.39 Å, CN = 12), Nb^{5+} (0.64 Å, CN = 6)), the introduction of A-site ions with smaller ionic radii such as Bi^{3+} (1.17 Å, CN = 12) and B-site ions with larger ionic radii such as $(Zn_{0.5}Sn_{0.5})^{3+}$ (0.69 Å, CN = 6) is conducive to reducing the tolerance factor, thus stabilizing antiferroelectricity and improving ESP. On the other hand, the lower polarizability of Zn^{2+} (1.017 Å^3)/Sn^{4+} (1.798 Å^3) compared to that of Nb^{5+} (3.10 Å^3) brings about a firmer ionic bonding [21], greatly contributing to the occurrence of short-range-ordered

polar clusters, which results in a depressed P_r. The hybridization of Bi 6p and O 2p orbitals could boost the polarity of the A-sites, balance the low polarity caused by the addition of low polarity ions (Zn^{2+}, Sn^{4+}) at B-sites, and maintain a high P_{max}. Based on these aforementioned considerations, a novel series of NN-based ceramic systems, *x*BZS ceramics, was designed and synthesized. The enhancement of ΔP mainly originates from highly dynamic nanodomains, as evidenced by the piezoresponse force microscopy (PFM) and the high-resolution transmission electron microscopy (HRTEM). Improving E_b is mainly attributed to the enhanced insulation properties caused by the synergistic effect of grain size and second phase. Consequently, a high U of 3.14 J/cm^3 and a large η of 83.30% have been simultaneously achieved in 0.10BZS solid solutions. In addition, good temperature (20–100 ℃) and frequency (1–200 Hz) stabilities of the energy storage characteristics were also achieved. For practical applications, a high W_{dis} of 1.05 J/cm^3, a fast discharge time of 60.6 ns, and a high hardness of 5.49 GPa were also synchronously achieved. These consequences demonstrate that the 0.10BZS ceramics are promising lead-free materials for pulsed power capacitors.

2 Experimental procedure

The experimental processes and characterization methods of *x*BZS ceramics were provided in the Electronic Supplementary Material (ESM).

3 Results and discussion

Figure 1(a) exhibits the XRD patterns of *x*BZS ceramics at RT. As x increases, the phase transition, ranging from orthorhombic (x = 0.05) with the several AFE peaks of very low intensity (the red arrows in Fig. 1(a)) to the pseudo-cubic phase ($x \geqslant 0.05$), can be verified by the changes in the (110) and (200) diffraction peaks. Similar phenomenon has been reported in other NN-based systems [15,22]. Nevertheless, the local scale distortion that exists in the high symmetry phase (cubic) was not observed through XRD for the low detection

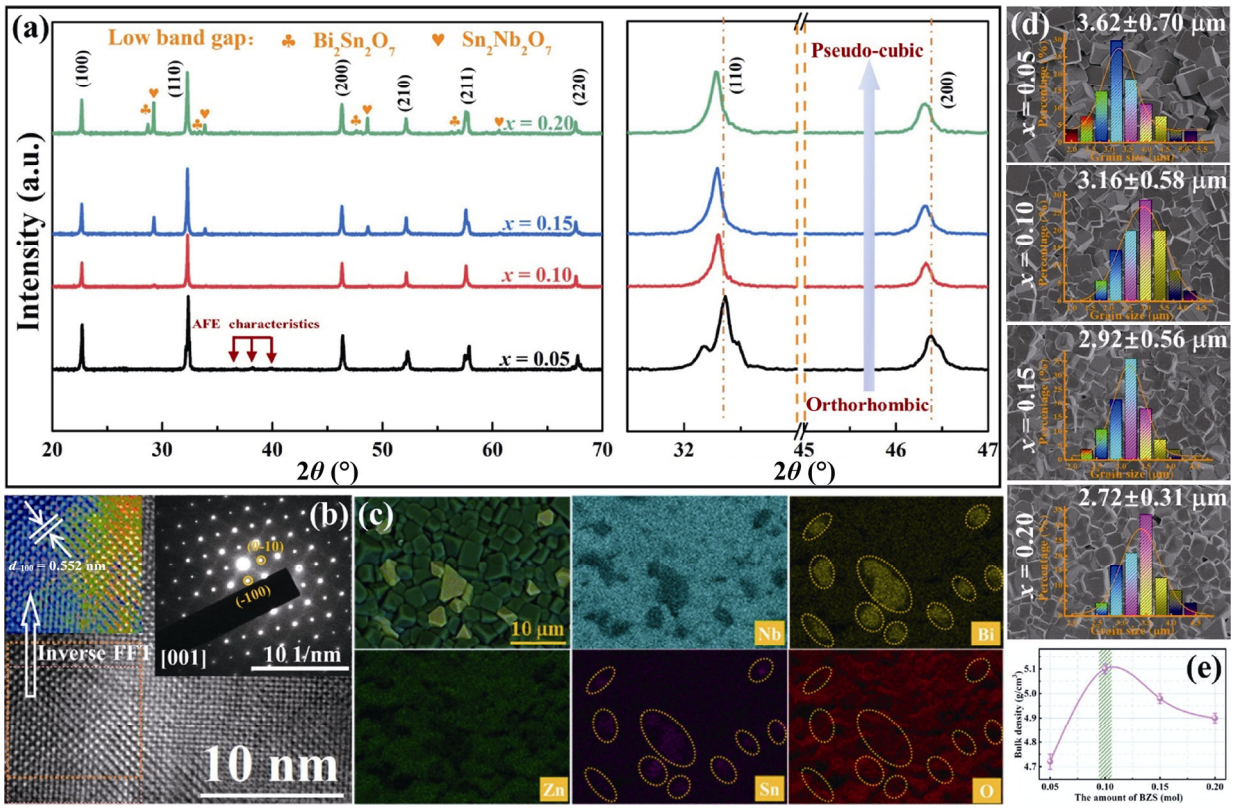

Fig. 1 (a) XRD patterns and enlargement images of *x*BZS ceramics. (b) SAED and HRTEM images of 0.10BZS ceramics (the inset shows the local inverse fast Fourier transform image). (c) Elemental mapping images of 0.20BZS ceramics. (d) Average grain sizes and standard deviations of *x*BZS ceramics. (e) Bulk densities of *x*BZS ceramics.

precision. Therefore, selected-area electron diffraction (SAED) and HRTEM patterns of 0.10BZS ceramics were applied to detect the local phase structure, as presented in Fig. 1(b). The interplanar spacing of $d_{-100} = 0.55(2)$ nm can be clearly found via HRTEM, inverse fast Fourier transformation (FFT), and SAED images, which is conform to the XRD data of the NN ceramics (tetragonal phase, PDF#73-1106), indicating that the local tetragonal phase exists in the 0.10BZS ceramics. Particularly, the secondary phases of $Sn_2Nb_2O_7$ (~2.30 eV) [23] and $Bi_2Sn_2O_7$ (~2.72 eV) [24] with a low band gap (~3.20 eV, pure NN [4]) are observed as the BZS content increases. To further confirm the existence of the second phases, Fig. 1(c) and Fig. S1 in the ESM show the elemental mapping of the 0.20BZS ceramics. The atomic density of the Nb element in $Sn_2Nb_2O_7$ and $Bi_2Sn_2O_7$ are lower than that of NN ceramics, which causes the content of Nb to be missing and minor. In contrast, the Bi, Sn, and O elements are enriched in the marked area, resulting in higher atomic densities. These results further verify the existence of the second phases of $Sn_2Nb_2O_7$ and $Bi_2Sn_2O_7$. Generally, the appearance of the intrinsic factors such as the low band gap second phase does not immediately deteriorate the E_b of the ceramics [25], and their E_b values are also influenced by extrinsic factors like the grain size and porosity. The local microstructures and grain size distribution images were acquired to further verify the source of high E_b, as exhibited in Fig. 1(d). All the as-prepared specimens present the dense microstructures, and the mean grain size decreases from 3.62 to 2.72 μm with increasing x. Decreasing the grain size (high densities of the grain boundaries) may be due to that the presence of the second phases further inhibits the migration of grain boundary. Generally, the thermal breakdown is one of the major contributors to the breakdown process of ceramics, which is caused by the deteriorating conductive leakage current [26]. Herein, the standard deviations and bulk densities of all samples are provided to further study the main factors of improving E_b. As shown in Fig. 1(d), although the significantly reduced standard deviation values in xBZS ceramics are conducive to achieving a uniform local electric field distribution and reducing the leakage current density, the E_b shows the highest value under the $x = 0.10$ composition, which may be caused by the deteriorated microstructure of this system at high contents (pores and secondary phases). Meanwhile, decreasing average grain size and increasing bulk density (Fig. 1(e)) in 0.10BZS ceramics also provide strong evidence. Therefore, the dense microstructure, small grain size, and high bulk density in 0.10BZS ceramics are conducive to achieving a large E_b.

The temperature-dependent dielectric constant (ε_r) and loss ($\tan\delta$) of the xBZS ceramics are shown at various frequencies (Fig. 2(a) and Fig. S2 in the ESM). A sharp phase transition peak ascribed to the first-order phase transition between R (AFE, space group *Pmnm*) and P phases [22] can be observed in 0.05BZS ceramics. The small hump of 0.05BZS ceramics at low temperatures is caused by a second-order AFE-to-AFE transformation [27]. With increasing x, the temperature of the maximum ε (T_m) decreased from 243 to −95 ℃, and ε_r first increased (from 552.56 to 879.41) and then decreased (from 879.41 to 639.77) under RT (Fig. 2(b)). Based on the research of Qu *et al*. [28], $NaNbO_3$–$BiMeO_3$ perovskite solid solutions can be divided into two types. The first type is that the concentration of $BiMeO_3$ dependence of the T_{max} is rather smooth, and the ε_{max} is sharp. The second type is that the T_{max} value suddenly drops, and ε_{max} shows a dramatic diffusion as the $BiMeO_3$ concentration increases to a certain value. With the further increasing $BiMeO_3$ content, the decreasing trend of T_{max} becomes slow. Although a significantly reduced T_m will destroy the polarization and then decrease the P_{max} values, it will also significantly reduce the large P_r of the NN ceramics, resulting in a higher polarization difference ($\Delta P = P_{max} - P_r$), which is advantageous for obtaining excellent ESP. The decreasing T_m is due to the weakened bonding in the [NbO_6] octahedron [28]. The increasing ε_r at low x content implies that the Bi^{3+} ions were dominant (hybridization between the Bi^{3+} 6p and O^{2-} 2p orbitals can cause large polarization) at A-sites. As x further increases, the low-polarization (Zn^{2+}, Sn^{4+}) ions at B-sites also increases, thereby suppressing the increasing ε_r. In addition, the broadened and weakened dielectric peaks (Fig. S2 in the ESM) provide strong evidence for the enhanced relaxor characteristics, which can also be verified by a reduction in intensity and a broadening of the Raman spectroscopy peaks. Typical multiple-peak features in the range of 100–300 cm^{-1} can be seen on the Raman spectra for 0.05BZS samples in Fig. S3 in the ESM, which may be related to the unique structure of the AFE P phase with its complex octahedral tilting behaviors. Meanwhile, it can be found that all peaks shifted to lower wavenumber as well as a decreased peak intensity, indicating that the polarity of the basic

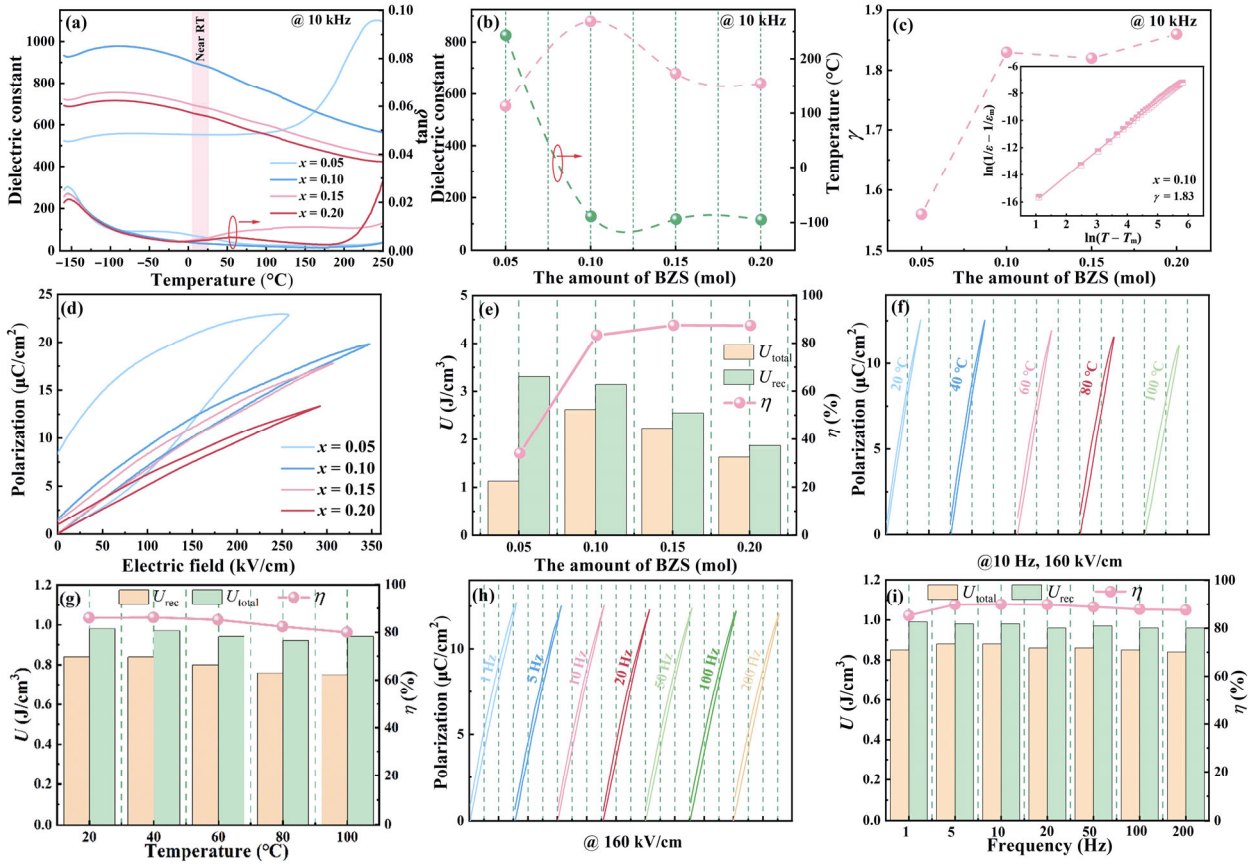

Fig. 2 (a) ε_r and tanδ of xBZS ceramics as a function of temperature, and f = 10 kHz. (b, c) ε_r, T_m, and γ vs. x for xBZS ceramics. (d) Unipolar P–E loops at various electrical fields of xBZS ceramics. (e) U_{rec}, U_{total}, and η for xBZS ceramics at critical electric fields. (f)–(i) Stabilities (temperature and frequency) of 0.10BZS ceramics.

perovskite unit cells is decreased (the increasing peak intensity of 0.20BZS ceramics may be caused by the appearance of the second phase). With increasing x, the intensity gradually weakened, the wavenumber decreased, and the width increased in Raman peaks with increasing x suggest a gradually decreased polarity, a weakening bond between B-site cations and oxygen, and an increased structural disorder, respectively [16]. These features should be compatible with the appearance of the macroscopic relaxor behavior. The modified Curie law is employed to further characterize the relaxor behavior of this system and the diffuseness degree γ as described by Eq. (4) [29,30]:

$$\frac{1}{\varepsilon_r} - \frac{1}{\varepsilon_m} = \frac{(T - T_m)^\gamma}{C} \tag{4}$$

where ε_m denotes the maximum ε_r at T_m, and C is a constant. The range of the γ value is between 1 (complete FE) and 2 (complete RFE). γ increased from 1.56 to 1.86 with the increasing BZS (Fig. 2(c)), which is consistent with the above analysis. In xBZS ceramics, Bi^{3+}, Zn^{2+}, and Sn^{4+} ions with various valence and radii hold the A and B-sites of the NN ceramic, which breaks the long-range order of the local electrical fields and local elastic fields, thus causing an enhanced relaxor phenomenon. In short, the ultra-low tanδ values (~0.30%), large ε_r (~879.41), and enhanced relaxor characteristics in 0.10BZS ceramics are conducive to achieving excellent ESP.

Figures 2(d) and 2(e) show the unipolar P–E loops and energy-storage behaviors of xBZS ceramics at their E_b. Typical AFE characteristics are presented in 0.05BZS ceramics (Fig. S4(a) in the ESM), indicating that the introduction of low content BZS can improve the stability of the AFE P phase. However, a large polarization hysteresis can still be found in NN-based ceramics. With a further increasing BZS content, the addition of the non-isovalent Bi^{3+} and (Ni^{2+}, Sn^{4+}) to the A and B-sites, respectively, causes a mismatch strain and local charge imbalance, resulting in a local random field that can destroy the long-range order availability into nano polar clusters and give rise to a strong relaxor

behavior. Analogous phenomena are also observed in other like-relaxor antiferroelectric ceramics [19]. In AFE ceramics, due to the opposite polarization of adjacent dipoles, they can be reoriented only under a large enough external electric field. Most of the AFE domains can turn into long-range ordered FE domains at a large applied electric field, which is extremely conducive to boosting P_{max}. Due to the presence of FE phase, however, their P_r was large, leading to the low U_{rec} and η. With increasing x, the enhancing relaxor behavior further alleviates the FE phase (Fig. 2(d)). As a result, a large U of 3.14 J/cm^3 and a high η of 83.3% are acquired in 0.10BZS ceramics, which are enhanced by 424% and 338% over unmodified NN ceramics in the previous work [31], respectively. Figure 3(a) provides a comparison of the energy storage characteristics (breakdown strength, energy density, and efficiency) of this work with other systems [16,18,28,32–34]. Obviously, 0.10BZS ceramics present a more excellent comprehensive characteristic. To further measure the energy storage performance of the 0.10BZS ceramics, the stabilities (temperature and frequency) of the ceramics are also carried out at 160 kV/cm, as shown in Figs. 2(f)–2(i). Concerning the temperature stability, as the temperature increases, the U_{rec} value gradually decreases from 0.84 to 0.75 J/cm^3 (variation of U_{rec} $\leqslant$ 10.72%), and η decreases from 86% to 80%. Decreasing U_{rec} and η may be due to the decreasing P_{max} and heat accumulation at high temperature. Similarly, 0.10BZS ceramics showed outstanding frequency stability (variation of U_{rec} $\leqslant$ 4.6% in 1–200 Hz). This good energy storage stability can probably be ascribed to the dense microstructure and enhanced relaxor behavior in 0.10BZS ceramics [35].

For actual applications, the charge/discharge behaviors of 0.10BZS ceramics were also assessed. Figures 4(a) and 4(b) demonstrate the overdamped discharge curves and W_{dis} ($W_{dis} = R\int i^2(t)\mathrm{d}t / V$, where V (0.628 mm^3) represents the volume of the samples, and R (210 Ω) is the load resistance) dependence of the discharge time under different electrical fields of 0.10BZS ceramics. The electrical field dependence of W_{dis} and $t_{0.9}$ values is introduced in the inset of Fig. 4(a). As the electric field increases, the W_{dis} increases from 0.012 to 1.05 J/cm^3, while the small discharge time $t_{0.9}$ has slight fluctuations around 60.6 ns. The overdamped discharge curves under different temperature at 180 kV/cm are shown in Fig. 4(c). With an increasing temperature, the peak current remains at a relatively constant value, indicating an excellent temperature stability of the ceramics (as displayed in the inset of Fig. 4(c)). Figure 4(d) shows that as the temperature increases from 20 to 140 ℃, the W_{dis} decreases from 0.78 to 0.69 J/cm^3 (variation less than 12%) owing to the changes in P_{max}, and $t_{0.9}$ decreases from 60.2 to 49.8 ns. This excellent charge/discharge behaviors may be mainly due to the enhanced E_b and highly dynamic polar nanoregions (PNRs) [36], indicating that the 0.10BZS ceramics are expected to be a potentially promising candidate for pulse power capacitors.

The evaluation of hardness properties is also important due to the severe external conditions in practical applications. Figures 5(a_1) and 5(a_2) show the typical load–displacement curves of xBZS (x = 0.00 and 0.10) ceramics sintered at their optimal sintering temperatures, which is obtained by the nanoindentation test. The loading and unloading curves were continuous and smooth for 0.00BZS and 0.10BZS ceramics, indicating

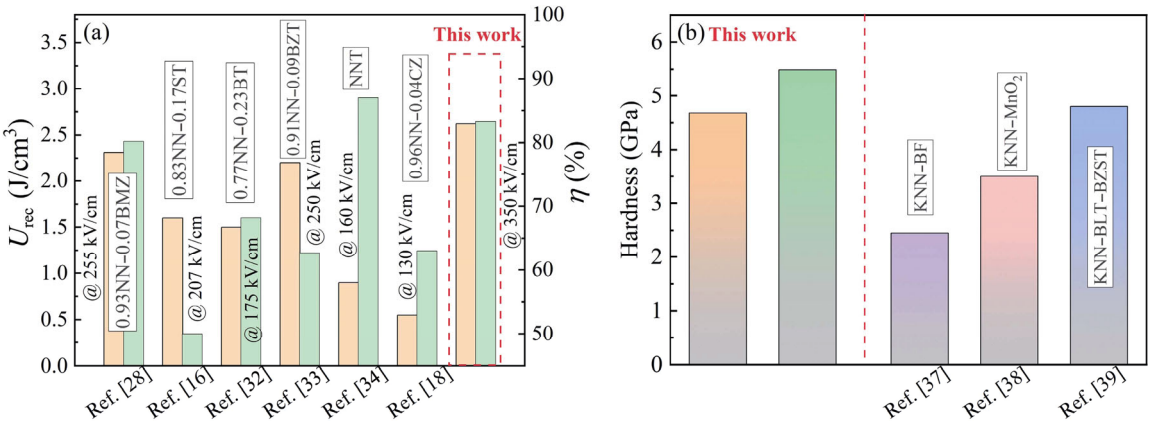

Fig. 3 (a) Comparison of energy storage properties between 0.10BZS ceramics and other reported NN-based ceramics. (b) Comparison of the hardness of xBZS (x = 0.00 and 0.10) ceramics and other lead-free ceramics.

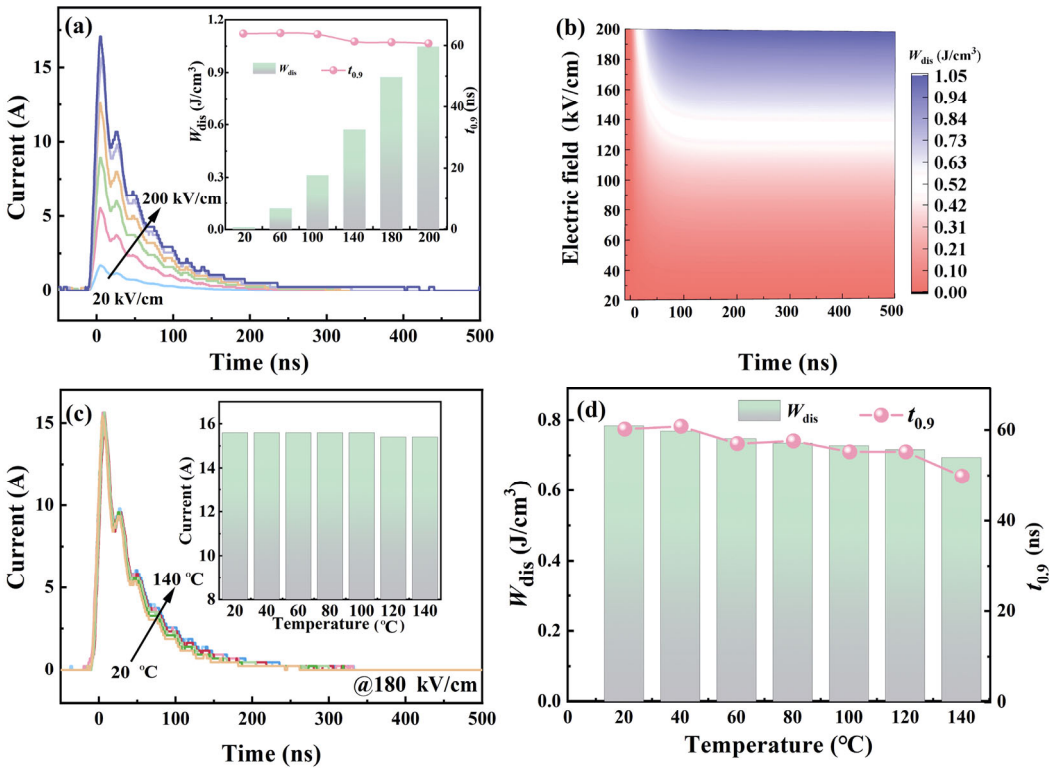

Fig. 4 (a) Overdamped discharge waveforms, (b) variation of W_{dis} for 0.10BZS ceramics vs. various electric field. (c) Overdamped discharge waveforms, (d) corresponding W_{dis} and $t_{0.9}$ for 0.10BZS ceramics at various temperatures under an applied electric field of 180 kV/cm.

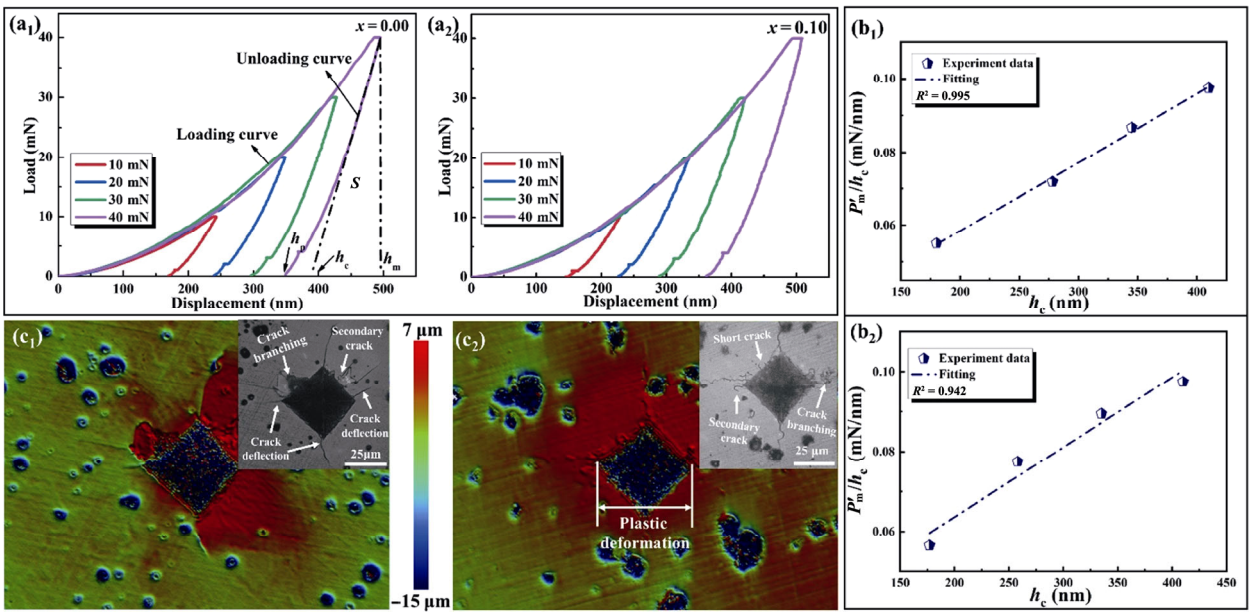

Fig. 5 (a_1, a_2) Load–displacement curves at different peak loads; (b_1, b_2) P'_m/h_c as a function of h_c; (c_1, c_2) 3D morphologies of Vickers indentation and cracks of *x*BZS (x = 0.00 and 0.10) ceramics.

that the research components underwent the elastic–plastic deformation without fracturing as the load was applied [6]. The parameters obtained by load–displacement curves, the indentation peak load (P'_m), contact depth (h_c), contact stiffness (S, the initial slope of the unloading curve), maximal depth (h_m), and remaining deformation depth (h_p) are listed in Table 1. The values of h_m, h_c, and h_p for *x*BZS (x = 0.00 and 0.10) ceramics

Table 1 Parameters of *x*BZS (*x* = 0.00 and 0.10) ceramics derived from the nanoindentation test

Component	P'_m (GPa)	h_m (nm)	h_c (nm)	h_p (nm)	S	H (GPa)	α_1 (mN/nm)	α_2 (nN/nm^2)	H_{01} (GPa)	H_{02} (GPa)
x = 0.00	9.988	236	180	160	0.0260	8.82	0.0254	0.000167	6.82	6.81
	19.994	350	278	250	0.0669	8.35			6.83	6.81
	29.940	428	345	300	0.1310	8.31			7.26	6.81
	39.922	509	410	365	0.2151	7.85			7.16	6.81
x = 0.10	9.993	227	173	155	0.2470	9.81	0.0158	0.000243	9.99	9.92
	19.984	335	256	230	0.0617	9.18			9.93	9.92
	29.999	428	338	295	0.1215	9.03			8.81	9.92
	39.978	508	412	365	0.2326	8.55			8.05	9.92

generally tend to increase as the peak load increases. However, the hardness, obtained by the nanoindentation test, has a tendency to decrease with the increasing peak load. It is worth noting that the evident hardness of a material obtained directly from nanoindentation is distinct from the real hardness. The proportional specimen resistance (PSR) model can be used as an appropriate method to interpret the nanoindentation data and describe the relation between the effective indentation load and the indentation dimension [37]:

$$\frac{P'_m}{h_c} = \alpha_1 + \alpha_2 h_c \tag{5}$$

$$H_{01} = \frac{P'_m - \alpha_1 h_c}{24.5 h_c^2} \tag{6}$$

$$H_{02} = \frac{\alpha_2}{24.5} \tag{7}$$

where α_1 and α_2 are two constants for the given materials (the relationship between P'_m/h_c and h_c was depicted in Figs. 5(b_1) and 5(b_2), and the coefficients of determination of R^2 are 0.995 and 0.942), and the values of H_{01} and H_{02} are the real hardness associated to α_1 and α_2, respectively. With increasing peak loads, H_{01} fluctuates around H_{02}. For size effects, the true hardness of the sample differs from the measured hardness. The 3D morphologies of typical pattern of indentations and cracks in BZS ceramics produced by Vickers are shown in Figs. 5(c_1) and 5(c_2). The samples of x = 0.10 have shorter cracks than those of x = 0.00 at the same load. Nevertheless, crack branching, secondary crack, and crack deflection can be clearly found in the inset of Fig. 5(c_1), which might be due to a deteriorating of the microstructure. According to the average length based on diagonals (d) (Table S1 in the ESM), hardness (H) can be calculated through the formula below: $H = 1.8544P'_m/d^2$, and the indentation load is 4.903 N. The hardness values of x = 0.00 and x = 0.10 are 4.68 and 5.49 GPa, respectively, indicating an enhancement of hardness, which is consistent with the results of the nanoindentation test. Therefore, the introduction of BZS can effectively improve the hardness of NN ceramics. Compared with other systems [38–40], 0.10BZS ceramics present superior hardness characteristics.

Figures 6(a)–6(d) show the impedance spectroscopy results for studying the conduction mechanism of *x*BZS ceramics. The normalized imaginary parts of the impedance (Z''/Z''_{max}) and modulus (M''/M''_{max}) of 0.10BZS ceramics have a significant frequency difference (Fig. S4(b) in the ESM), manifesting that grain and grain boundary responses of the samples are very different. Therefore, the impedance data are deconvoluted with the 2 equivalent random quantum circuits (RQCs), where the 2 RQCs represent grain and grain boundary. Decent correlations show in all samples. Generally, the resistance data of the grain and grain boundary conform to the Arrhenius relationship can be expressed as follows [41]:

$$R = R_0 \exp(E_{rel}/k_B T) \tag{8}$$

where the value of R is the resistance, R_0 is a constant, k_B is the Boltzmann constant, and E_{rel} is the resistance activation energy. Various relaxor processes seem to coexist in ceramics, which contain a number of various energy barriers due to point defects (cation and oxygen vacancies) appearing during technological processes. In general, oxygen vacancies have reported activation energies in the range of 0.3–0.5 eV for single-ionized oxygen vacancies and 0.6–1.2 eV for doubly-ionized oxygen vacancies. Cation vacancies are quenched defects under low temperatures, and such vacancies could turn mobile at higher temperatures, with large E_{rel} (> 2.0 eV). In this work, the calculated resistance activation energies (E_g) of the grain in *x*BZS solid solutions are 0.73, 1.74, 0.86, and 1.20 eV, and the

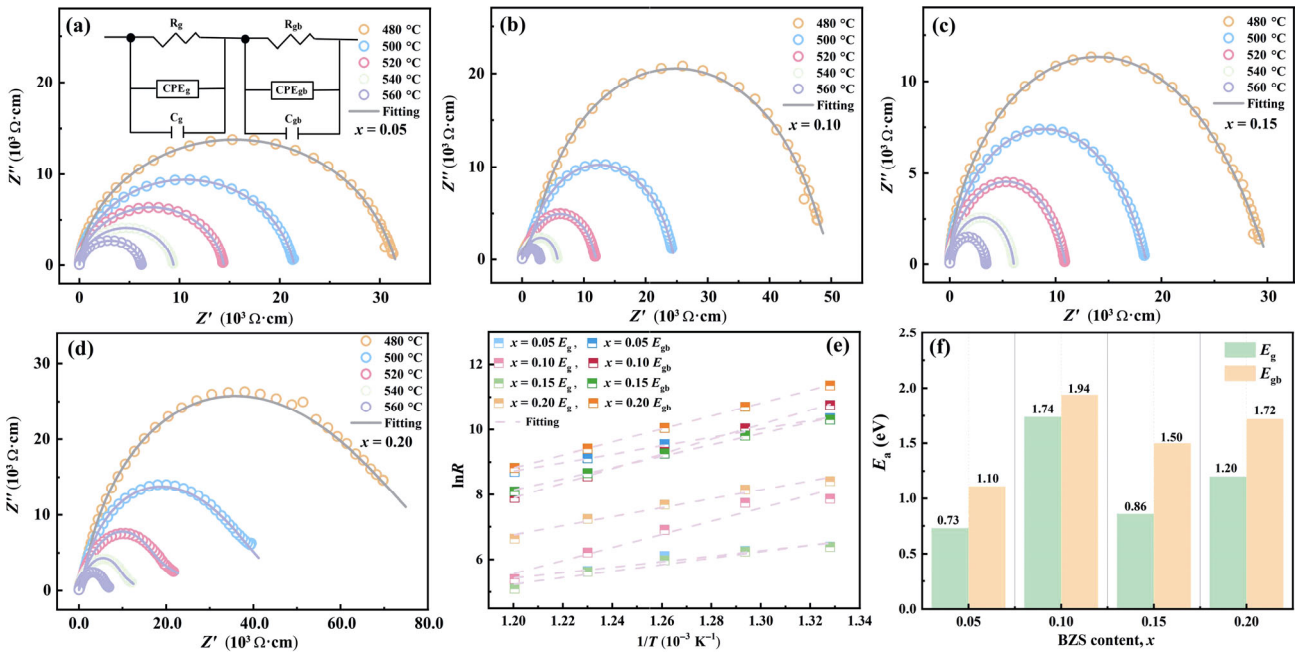

Fig. 6 (a)–(d) Complex impedance plots of *x*BZS ceramics measured under different temperatures from 480 to 560 ℃. (e) Arrhenius fitting of grain and grain boundary resistance data of *x*BZS ceramics. (f) Changes in E_g and E_{gb} at different components.

resistance activation energies (E_{gb}) of the grain boundary are 1.10, 1.94, 1.50, and 1.72 eV. Obviously, the E_{gb} values are larger than those of the E_g for all components, indicating that the grain boundary resistance is dominant at high temperature. The significantly increased resistance activation energy can be explained by the following points: First, oxygen vacancies facilitate the appearance of dipoles formed with an adjacent host ion and enlarge the rattling space available for dipole vibration, which results in the short-range hopping of the ions and produces the relaxor behavior. Second, the oxygen ion jumps between the vacancies are considered to be responsible for the transition from short-range to long-range hopping, resulting in the marked ion conductivity [42]. This type of high grain and grain boundary activation energy differences has also reported in other energy storage ceramic systems [41]. Generally, a higher E_{gb} in 0.10BZS ceramics means that there is a decrease of the free oxygen vacancy at grain border. Therefore, the higher barrier of the oxygen vacancy hopping in the grain boundary compensates for the grain boundary defect, and is beneficial to acquiring high E_b [31,43]. Notably, a relatively high E_{gb} in 0.20BZS ceramics does not achieve the ideal E_b (see Fig. 2(d)), which may be due to the influence of the second phase (see Fig. 1(a)). Based on the Weibull distribution, the breakdown strength and Weibull modulus of all the as-prepared samples are given in Fig. S4(c) in the ESM. The shape parameter β of all the compositions is larger than 7, thus proving high reliability of the obtained E_b values.

To further reveal the origin of the excellent ESP of *x*BZS ceramics, the local microstructure observations for 0.05BZS and 0.10BZS ceramics were performed via HRTEM. The introduction of BZS further disrupts polar order and induces smaller sized domain feature. For instance, the large sized domains (~16–40 nm) with high barriers are obtained in 0.05BZS ceramics. More of the smaller sized domains (~1.0–1.8 nm) in 0.10BZS ceramics can be obtained, as indicated in Fig. 7(a). The smaller sized domains with the high dynamics and low energy barriers are extremely advantageous for achieving an excellent energy storage characteristic. In addition, the domain structures of 0.05BZS and 0.10BZS ceramics are also explored using vertical piezoresponse force microscopy (VPFM), as exhibited in Fig. 7(d). No signal is shown in the amplitude and phase pictures for 0.05BZS ceramics. This may be attributed to the transition from AFE to FE phase occurring in a high electric field (see Fig. S4(a) in the ESM) [44], which is the increased number of large domains with higher barriers in 0.05BZS ceramics than those of 0.10BZS ceramics. In contrast, the nanoscale domains are detected in 0.10BZS ceramics via the

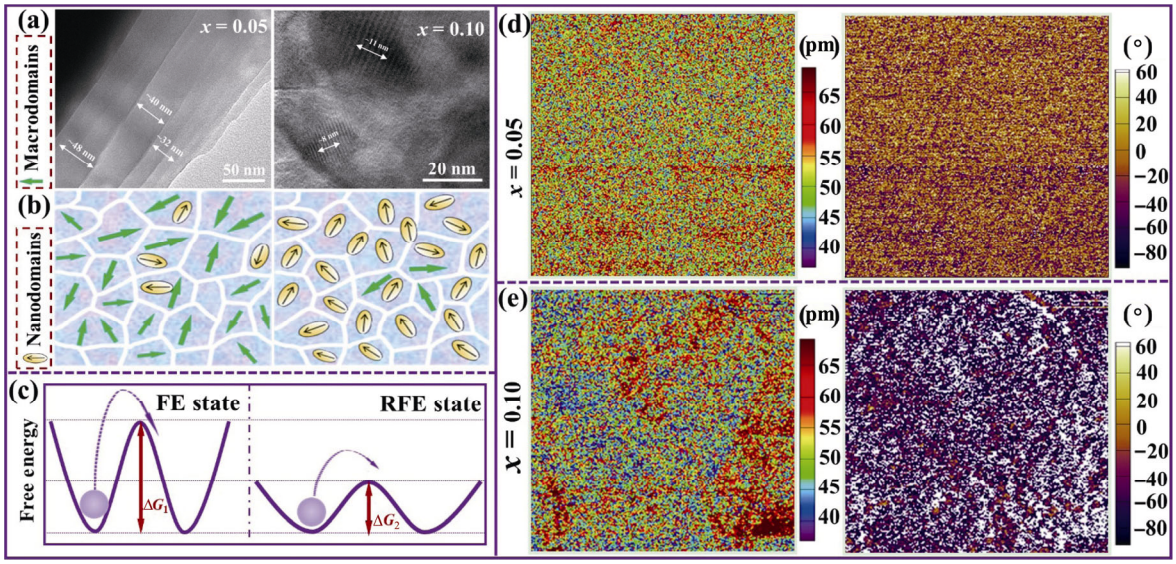

Fig. 7 (a) HRTEM images of domain morphology for *x*BZS (x = 0.05 and 0.10) ceramics. (b, c) Schematic diagram of detailed domain structure variation of the process. (d, e) Vertical piezoelectric force microscopy (VPFM) images for *x*BZS (x = 0.05 and 0.10) ceramics.

comparison of amplitude and phase images (Fig. 7(e)). The incorporation of non-isovalent Bi^{3+} and (Zn^{2+}, Sn^{4+}) ions at A- and B-sites into the host lattice NN results in a local charge imbalance and mismatch strain, causing the formation of PNRs and random fields. Therefore, some PNRs combine into percolation clusters, and then develop into nano-domains [25]. These nanodomains have both a small hysteresis loss and a low switching electrical field because of their high dynamics and low energy barriers (Figs. 7(b) and 7(c)), which contribute to achieving a weak dielectric nonlinearity and slender *P*–*E* hysteresis loops [12].

To better understand the domain structure in *x*BZS ceramics, local poling experiments are employed, as illustrated in Fig. 8. A negative DC voltage of −30.0 V was applied to the tip of the sample with a region of 3.0 μm × 3.0 μm, and then different positive voltages (+7.5, +15.0, +22.5, and +30.0 V) was applied on the four square regions of 1.0 μm × 1.0 μm, to describe the out-of-plane phase patterns during local poling, as shown in Figs. 8(a_1) and 8(b_1). For 0.05BZS ceramics, almost no switching domains are shown under +7.5 and +15.0 V. While the poling voltage increases from +15.0 to +30.0 V, although the switched part of PNRs gradually increases, the switching is yet not complete (Fig. 8(a_1)). In contrast, a low poling voltage of +7.5 V can switch the majority of the nanodomains in 0.10BZS ceramics, indicating low switching energy barriers (Fig. 8(b_1)) [45]. Relaxor behavior of the switched domains was also investigated to evaluate the polarization response, as shown in Figs. 8(a_2)–8(b_3). The switching domains in 0.05BZS ceramics did not change remarkably after the relaxor time of 30 min. On the contrary, for 0.10BZS ceramics, the switched nanodomains can almost come back to their initial state in an extremely short time (~5 min) (Fig. 8(b_2)), indicating highly dynamic nanodomains in this system. Consequently, the nanodomains with low energy barriers and high dynamics are obtained simultaneously, which allows a small P_r and a low hysteresis loss, resulting in an enhanced ESP.

4 Conclusions

A novel antiferroelectric ceramic NN-based solid solution with relaxor properties and an enhanced ESP was successfully designed and fabricated via composition regulation. Enhancement of the ESP was mainly derived from the improved ΔP and E_b. The enhanced ΔP mainly originated from highly dynamic nanodomains, as demonstrated by PFM. The improving E_b is primarily attributed to the synergistic effect of grain size and second phase. Consequently, a large energy storage density of 3.14 J/cm^3, a high energy efficiency of 83.30%, and a good hardness of 5.49 GPa were simultaneously achieved in the 0.10BZS ceramics. In addition, they also had good thermal (20–100 ℃) and excellent frequency (1–200 Hz) stability. All these outcomes demonstrate that 0.10BZS ceramics are

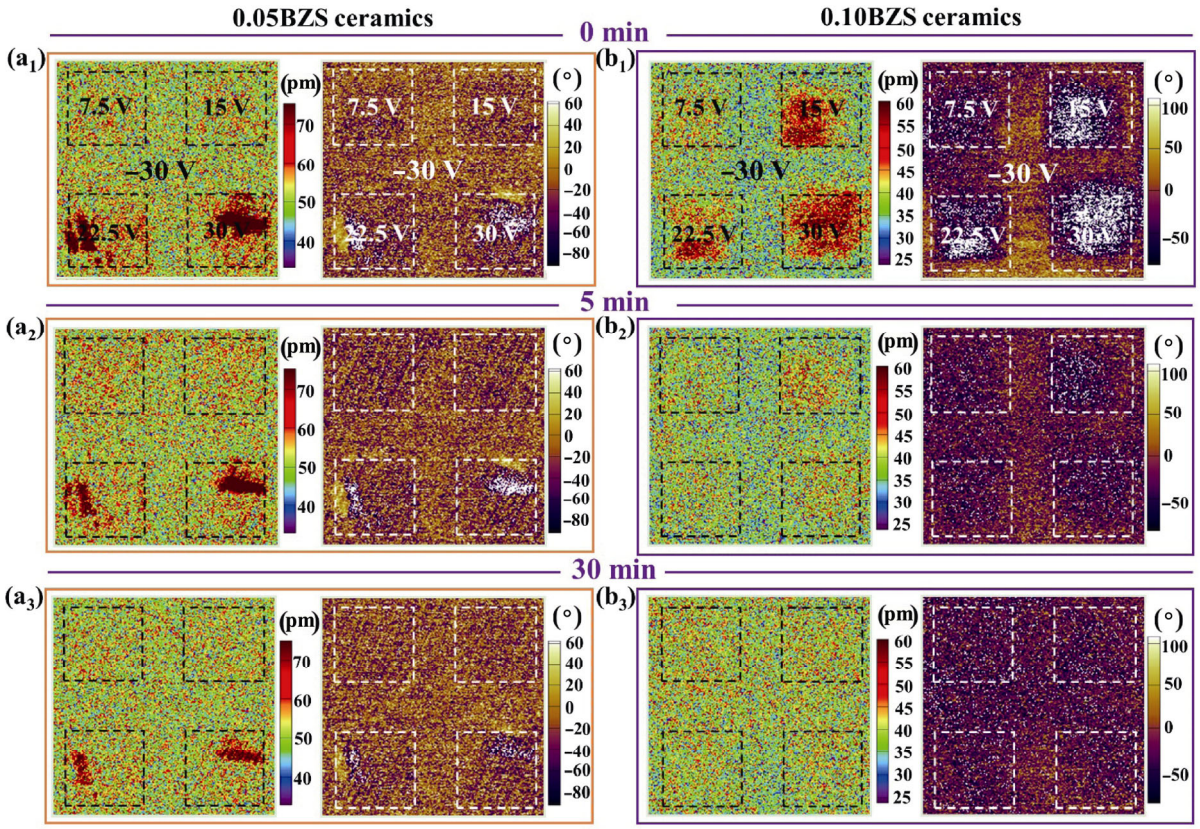

Fig. 8 PFM amplitude and phase pictures after poling treatment with varying voltages and relaxor periods of (a) 0.05BZS and (b) 0.10BZS ceramics.

potentially promising lead-free materials for pulsed power capacitors.

Acknowledgements

This work was supported by the National Natural Science Foundation of China (Nos. 12064007, 11664008, and 61761015), the Natural Science Foundation of Guangxi (Nos. 2018GXNSFFA050001, 2017GXNSFDA198027, and 2017GXNSFFA198011), and High Level Innovation Team and Outstanding Scholar Program of Guangxi Institutes.

Declaration of competing interest

The authors have no competing interests to declare that are relevant to the content of this article.

Electronic Supplementary Material

Supplementary material is available in the online version of this article at https://doi.org/10.1007/s40145-022-0566-6.

References

[1] Wang G, Lu ZL, Li Y, *et al*. Electroceramics for high-energy density capacitors: Current status and future perspectives. *Chem Rev* 2021, **121**: 6124–6172.

[2] Chu B, Zhou X, Ren K, *et al.* A dielectric polymer with high electric energy density and fast discharge speed. *Science* 2006, **313**: 334–336.

[3] Zhao PY, Cai ZM, Chen LL, *et al*. Ultra-high energy storage performance in lead-free multilayer ceramic capacitors via a multiscale optimization strategy. *Energy Environ Sci* 2020, **13**: 4882–4890.

[4] Qi H, Xie AW, Tian A, *et al.* Superior energy-storage capacitors with simultaneously giant energy density and efficiency using nanodomain engineered $BiFeO_3$–$BaTiO_3$–$NaNbO_3$ lead-free bulk ferroelectrics. *Adv Energy Mater* 2019, **10**: 1903338.

[5] Han K, Luo NN, Mao SF, *et al*. Ultrahigh energy-storage density in A-/B-site co-doped $AgNbO_3$ lead-free antiferroelectric ceramics: Insight into the origin of antiferroelectricity. *J Mater Chem A* 2019, **7**: 26293–26301.

[6] Xing J, Huang Y, Xu Q, *et al.* Realizing high comprehensive energy storage and ultrahigh hardness in lead-free ceramics. *ACS Appl Mater Interfaces* 2021, **13**: 28472–28483.

[7] Li X, Cheng Y, Wang F, *et al.* Enhancement of energy

storage and hardness of $(Na_{0.5}Bi_{0.5})_{0.7}Sr_{0.3}TiO_3$-based relaxor ferroelectrics via introducing $Ba(Mg_{1/3}Nb_{2/3})O_3$. *Chem Eng J* 2022, **431**: 133441.

[8] Luo BC, Wang XH, Tian EK, *et al*. Enhanced energy-storage density and high efficiency of lead-free $CaTiO_3$–$BiScO_3$ linear dielectric ceramics. *ACS Appl Mater Interfaces* 2017, **9**: 19963–19972.

[9] Dai Z, Xie J, Liu W, *et al.* Effective strategy to achieve excellent energy storage properties in lead-free $BaTiO_3$-based bulk ceramics. *ACS Appl Mater Interfaces* 2020, **12**: 30289–30296.

[10] Luo NN, Han K, Cabral MJ, *et al*. Constructing phase boundary in $AgNbO_3$ antiferroelectrics: Pathway simultaneously achieving high energy density and efficiency. *Nat Commun* 2020, **11**: 4824.

[11] Yuan QB, Li G, Yao FZ, *et al*. Simultaneously achieved temperature-insensitive high energy density and efficiency in domain engineered $BaTiO_3$–$Bi(Mg_{0.5}Zr_{0.5})O_3$ lead-free relaxor ferroelectrics. *Nano Energy* 2018, **52**: 203–210.

[12] Li X, Chen XL, Sun J, *et al*. Novel lead-free ceramic capacitors with high energy density and fast discharge performance. *Ceram Int* 2020, **46**: 3426–3432.

[13] Zhou XF, Qi H, Yan ZN, *et al*. Superior thermal stability of high energy density and power density in domain-engineered $Bi_{0.5}Na_{0.5}TiO_3$–$NaTaO_3$ relaxor ferroelectrics. *ACS Appl Mater Interfaces* 2019, **11**: 43107–43115.

[14] Qi H, Zuo RZ, Xie AW, *et al*. Ultrahigh energy-storage density in $NaNbO_3$-based lead-free relaxor antiferroelectric ceramics with nanoscale domains. *Adv Funct Mater* 2019, **29**: 1903877.

[15] Dong XY, Li X, Chen XL, *et al*. High energy storage density and power density achieved simultaneously in $NaNbO_3$-based lead-free ceramics via antiferroelectricity enhancement. *J Materiomics* 2021, **7**: 629–639.

[16] Xie AW, Qi H, Zuo RZ. Achieving remarkable amplification of energy-storage density in two-step sintered $NaNbO_3$–$SrTiO_3$ antiferroelectric capacitors through dual adjustment of local heterogeneity and grain scale. *ACS Appl Mater Interfaces* 2020, **12**: 19467–19475.

[17] Ye JM, Wang GS, Chen XF *et al.* Enhanced antiferroelectricity and double hysteresis loop observed in lead-free $(1-x)NaNbO_3$–$xCaSnO_3$ ceramics. *Appl Phys Lett* 2019, **114**: 122901.

[18] Liu ZY, Lu JS, Mao YQ, *et al.* Energy storage properties of $NaNbO_3$–$CaZrO_3$ ceramics with coexistence of ferroelectric and antiferroelectric phases. *J Eur Ceram Soc* 2018, **38**: 4939–4945.

[19] Ye JM, Wang GS, Zhou MX, *et al.* Excellent comprehensive energy storage properties of novel lead-free $NaNbO_3$-based ceramics for dielectric capacitor applications. *J Mater Chem C* 2019, **7**: 5639–5645.

[20] Luo NN, Han K, Zhuo FP, *et al*. Design for high energy storage density and temperature-insensitive lead-free antiferroelectric ceramics. *J Mater Chem C* 2019, **7**: 4999–5008.

[21] Chen XL, Li X, Sun J, *et al.* Achieving ultrahigh energy storage density and energy efficiency simultaneously in barium titanate based ceramics. *Appl Phys A* 2020, **126**: 146.

[22] Zhou MX, Liang RH, Zhou ZY, *et al.* Superior energy storage properties and excellent stability of novel $NaNbO_3$-based lead-free ceramics with A-site vacancy obtained via a Bi_2O_3 substitution strategy. *J Mater Chem A* 2018, **6**: 17896–17904.

[23] Hosogi Y, Shimodaira Y, Kato H, *et al.* Role of Sn^{2+} in the band structure of SnM_2O_6 and $Sn_2M_2O_7$ (M = Nb and Ta) and their photocatalytic properties. *Chem Mater* 2008, **20**: 1299–1307.

[24] Hu CH, Yin XH, Wang DH, *et al*. First-principles studies of electronic, optical, and mechanical properties of γ-$Bi_2Sn_2O_7$. *Chin Phys B* 2016, **25**: 067801.

[25] Xing J, Huang YL, Wu B, *et al.* Energy storage behavior in $ErBiO_3$-doped $(K,Na)NbO_3$ lead-free piezoelectric ceramics. *ACS Appl Electron Mater* 2020, **2**: 3717–3727.

[26] Yang ZT, Du HL, Jin L, *et al.* Realizing high comprehensive energy storage performance in lead-free bulk ceramics via designing an unmatched temperature range. *J Mater Chem A* 2019, **7**: 27256–27266.

[27] Chao LM, Hou YD, Zheng MP, *et al*. High dense structure boosts stability of antiferroelectric phase of $NaNbO_3$ polycrystalline ceramics. *Appl Phys Lett* 2016, **108**: 212902.

[28] Qu N, Du HL, Hao XH. A new strategy to realize high comprehensive energy storage properties in lead-free bulk ceramics. *J Mater Chem C* 2019, **7**: 7993–8002.

[29] Uchino K, Nomura S. Critical exponents of the dielectric constants in diffused-phase-transition crystals. *Ferroelectrics* 1982, **44**: 55–61.

[30] Ji HF, Wang DW, Bao WC, *et al*. Ultrahigh energy density in short-range tilted NBT-based lead-free multilayer ceramic capacitors by nanodomain percolation. *Energy Storage Mater* 2021, **38**: 113–120.

[31] Chen HY, Shi JP, Chen XL, *et al.* Excellent energy storage properties and stability of $NaNbO_3$–$Bi(Mg_{0.5}Ta_{0.5})O_3$ ceramics by introducing $(Bi_{0.5}Na_{0.5})_{0.7}Sr_{0.3}TiO_3$. *J Mater Chem A* 2021, **9**: 4789–4799.

[32] Yang ZT, Du HL, Jin L, *et al.* A new family of sodium niobate-based dielectrics for electrical energy storage applications. *J Eur Ceram Soc* 2019, **39**: 2899–2907.

[33] Fan YZ, Zhou ZY, Liang RH, *et al*. Designing novel lead-free $NaNbO_3$-based ceramic with superior comprehensive energy storage and discharge properties for dielectric capacitor applications via relaxor strategy. *J Eur Ceram Soc* 2019, **39**: 4770–4777.

[34] Bian JJ, Otonicar M, Spreitzer M, *et al*. Structural evolution, dielectric and energy storage properties of $Na(Nb_{1-x}Ta_x)O_3$ ceramics prepared by spark plasma sintering. *J Eur Ceram Soc* 2019, **39**: 2339–2347.

[35] Huan Y, Wei T, Wang XZ, *et al.* Achieving ultrahigh energy storage efficiency in local-composition gradient-structured

ferroelectric ceramics. *Chem Eng J* 2021, **425**: 129506.

[36] Zhou MX, Liang RH, Zhou ZY, *et al*. Novel $BaTiO_3$-based lead-free ceramic capacitors featuring high energy storage density, high power density, and excellent stability. *J Mater Chem C* 2018, **6**: 8528–8537.

[37] Xie SX, Xu JG, Chen Y, *et al*. Indentation behavior and mechanical properties of tungsten/chromium co-doped bismuth titanate ceramics sintered at different temperatures. *Materials* 2018, **11**: 503.

[38] Yang ZT, Gao F, Du HL, *et al.* Grain size engineered lead-free ceramics with both large energy storage density and ultrahigh mechanical properties. *Nano Energy* 2019, **58**: 768–777.

[39] Zheng MP, Hou YD, Yan XD, *et al.* A highly dense structure boosts energy harvesting and cycling reliabilities of a high-performance lead-free energy harvester. *J Mater Chem C* 2017, **5**: 7862–7870.

[40] Wang XY, Venkataraman LK, Tan C, *et al*. Fracture behavior in electrically poled alkaline bismuth- and potassium- based lead-free piezoceramics using Vickers indentation. *Scripta Mater* 2021, **194**: 113647.

[41] Wu LW, Wang XH, Li LT. Lead-free $BaTiO_3$–$Bi(Zn_{2/3}Nb_{1/3})O_3$ weakly coupled relaxor ferroelectric materials for energy storage. *RSC Adv* 2016, **6**: 14273–14282.

[42] Liu LJ, Huang YM, Su CX, *et al.* Space-charge relaxation and electrical conduction in $K_{0.5}Na_{0.5}NbO_3$ at high temperatures. *Appl Phys A* 2011, **104**: 1047–1051.

[43] Sui JN, Fan HQ, Hu B, *et al*. High temperature stable dielectric properties and enhanced energy-storage performance of $(1-x)(0.85Na_{0.5}Bi_{0.5}TiO_3–0.15Ba_{0.8}Ca_{0.2}Ti_{0.8}Zr_{0.2}O_3)–xK_{0.5}Na_{0.5}NbO_3$ lead-free ceramics. *Ceram Int* 2018, **44**: 18054–18059.

[44] Gao J, Zhang YC, Zhao L, *et al*. Enhanced antiferroelectric phase stability in La-doped $AgNbO_3$: Perspectives from the microstructure to energy storage properties. *J Mater Chem A* 2019, **7**: 2225–2232.

[45] Yin J, Li CY, Wu B, *et al*. Defect-induced superior piezoelectric response in perovskite $KNbO_3$. *J Eur Ceram Soc* 2021, **41**: 2506–2513.